applied sciences

MDPI

Article

Research on the Vehicle Steering and Braking Stability Region

Xianbin Wang [1,*], Weifeng Li [1], Fugang Zhang [2], Zexuan Li [1] and Wenlong Bao [1]

[1] School of Civil Engineering and Transportation, Northeast Forestry University, Harbin 150040, China; lwf@nefu.edu.cn (W.L.); lizexuan@nefu.edu.cn (Z.L.); meihao18869@nefu.edu.cn (W.B.)
[2] Commercial Vehicle Development Institute of China FAW Jiefang Automobile Co., Ltd., Changchun 130062, China; zhangfugang@fawjiefang.com.cn
* Correspondence: xbwang@nefu.edu.cn; Tel.: +86-139-4605-2235

Abstract: Solving the stability region in the plane motion of vehicles has become a hot research topic in vehicle handling stability under extreme conditions, but there is still a lack of research on the stability region under steering and braking conditions. In this paper, a five-degree-of-freedom (5DOF) nonlinear dynamic model of a vehicle with braking torque introduced is established, and the model is transformed into an equivalent system by using the D'Alembert principle. Then, the equilibrium points of the equivalent system are solved by using an improved hybrid algorithm combining the genetic algorithm (GA) and sequential quadratic programming (SQP) method. According to the bifurcation characteristics of the equilibrium points, the boundary of the stability region at the given initial longitudinal velocity is determined, and the three-dimensional stability region is fitted. Finally, the stability region of the equivalent system and the original system are analyzed by the energy dissipation method, and the stability region determined by the equilibrium point bifurcation method is verified by simulation. The results show that as the braking torque increases, the number of equilibrium points increase to three from one, the equilibrium bifurcation method proposed in this paper can effectively solve the stability region of the equivalent system, and the solution results are consistent with the original system stability region. When the limited braking torque is 500 N·m and the initial longitudinal velocity increases from 30 m/s to 50 m/s, the absolute value of the front wheel steering angle at the boundary point changes from less than 0.02 rad to more than 0.02 rad.

Keywords: vehicle nonlinear dynamics; stability region; equilibrium point bifurcation method; steering and braking; energy dissipation method

Citation: Wang, X.; Li, W.; Zhang, F.; Li, Z.; Bao, W. Research on the Vehicle Steering and Braking Stability Region. *Appl. Sci.* **2023**, *13*, 7806. https://doi.org/10.3390/app13137806

Academic Editors: Edgar Sokolovskij and Vidas Žuraulis

Received: 20 April 2023
Revised: 29 June 2023
Accepted: 30 June 2023
Published: 2 July 2023

1. Introduction

With the application of nonlinear dynamics in the field of vehicle dynamics, the determination of stable regions in the plane motion of vehicles has become an important research field [1]. For the vehicle system, the external input (or driver) affects the dynamic stability of the system through acceleration, deceleration, and steering, which puts the vehicle in single or coupled working conditions. Many scholars have studied the plane motion stability of vehicles under various driving conditions through different nonlinear analysis methods.

Steering stability research of vehicles at a constant velocity was originally based on two-degree-of-freedom (2DOF) nonlinear vehicle model analysis. The steering angle bifurcation caused by tire lateral force saturation has been confirmed by many scholars. The band convergence region in the phase plane has been determined as the stable region of the system, and significant results have been achieved in the stability control of lateral motion [2–5]. Sadri et al. used the Lyapunov function method to analyze the lateral stability of vehicle steering [6], and in a follow-up study, Lyapunov exponents were also used to obtain the lateral stability region of the vehicle, which was an extension of the stability region obtained by using the Lyapunov function in the original study [7]. Rossa et al. combined the 2DOF nonlinear vehicle model with a simple driver model, analyzed the

Hopf bifurcation characteristics of vehicles with understeer and oversteer characteristics under steady steering and found different bifurcation forms of the system through the combination of different vehicle models and driver models, and found chaos in the driving simulator as well [8,9]. Steindl et al. found supercritical Hopf bifurcation of oversteer vehicles when studying the 2DOF nonlinear model [10].

Although the research based on the classical 2DOF nonlinear model of vehicles has achieved many research results, the model assumes that the longitudinal velocity remains unchanged and only considers the lateral force of the tires, without considering the impact of the longitudinal force of the tires on the system stability, which is not in line with the actual force situation of the tires in the actual driving of vehicles. Liu et al. introduced the longitudinal velocity into the vehicle model to establish a three-degree-of-freedom (3DOF) model and removed the assumption that the longitudinal velocity was constant [11]. Through a change of phase space trajectory, they pointed out that the essential feature of vehicle steering instability was the chaotic motion of the vehicle dynamics system. Masouleh et al. estimated the region of attraction (ROA) of the lateral dynamics of a 3DOF vehicle model through the sum of squares (SOS) programming algorithm [12]. Meng et al. put forward an energy dissipation method of vehicle plane motion and calculated the stability region of the 3DOF model. By comparison, it was proved that the energy dissipation method was more intuitive and easier to calculate than the Lyapunov exponents method [1]. In this study, the largest Lyapunov exponents and the sum of the Lyapunov exponents take 895,273 s (about 10 days) for numerical calculation. The total dissipation of energy takes 420 s for calculation.

Based on the research on 3DOF model steering conditions, Wang et al. established a five-degree-of-freedom (5DOF) vehicle nonlinear model incorporating driving torque, analyzed the impact of driving modes on vehicle stability under different steering angles [13], and obtained a two-dimensional bifurcation parameter set (driving stability region) under vehicle steering and driving conditions based on solving the equilibrium point of the 5DOF system [14]. Shi et al. used the Lyapunov exponents method and energy dissipation method to quantitatively analyze the stability region of the system under steering and driving conditions and obtained the stability region of state variables (lateral velocity and yaw rate) [15] and the stability region of system control parameters (front wheel angle and driving torque) [16], respectively. The different characteristics of dynamics between the high-degree-of-freedom model and the 2DOF model were revealed and explained. It was also proved that the maximum deviation of the energy dissipation method from the equilibrium point bifurcation method is less than 1.2%.

Braking is a common condition in vehicle driving, and many scholars have also studied its stability through nonlinear analysis methods. Based on considering the wheel slip dynamics, Olson et al. studied the longitudinal braking dynamics of a two-wheeled vehicle model coupled with the vehicle body and studied the variety of wheel slip rate when the braking torque changes through a bifurcation diagram, showing the whole process of how the system transits from stable braking to locking in one or two wheels, and then locking in two wheels [17]. Horiuchi et al. proposed an analysis method based on constrained bifurcation and continuity methods with the D'Alembert principle introduced, established a vehicle dynamics model including longitudinal velocity, lateral velocity, yaw rate and roll, and analyzed the bifurcation phenomenon caused by braking deceleration [18]. Chen et al. studied the 3DOF dynamic model combined with the Burckhardt tire model, studied the change of system equilibrium point under front/rear/four-wheel braking by the phase plane method, and obtained the stable region corresponding to the slip rate of the front and rear wheels when the vehicle turns to brake [19]. Zhu et al. considered engine braking in the 5DOF model and obtained the bifurcation diagram of the equilibrium point with the change of front wheel angle and longitudinal velocity through the phase plane method and static bifurcation theory [20]. Lai et al. constructed an 18-degree-of-freedom unified dynamic model of a vehicle chassis including three subsystems: a steering subsystem, braking subsystem and suspension subsystem, analyzed the influence of front and rear

wheel braking modes on vehicle driving stability by the phase plane analysis method, and found that front wheel braking is more stable than rear wheel braking [21]. A new model based on factors of the driver, vehicle and environment was developed to determine the 'safe stopping distance' of vehicles, and tested on real road conditions by using equipment placed on a vehicle [22].

It can be stated that, as a nonlinear dynamic system with multiple degrees of freedom, the steering instability mechanism of a vehicle has been basically recognized as a bifurcation phenomenon in a nonlinear system, and the instability mechanism under driving and steering conditions can also be explained by bifurcation theory. From the above research, it can be found that due to the particularity of braking dynamics, many scholars have focused on the design of controllers and the analysis of braking mechanisms based on simple vehicle models. When the system dimensions increase, it is necessary to simplify the model or improve the nonlinear analysis methods for analysis. However, there is still a lack of achievements in terms of analyzing or calculating the braking stability region. By systematically studying the vehicle steering and braking stability region, the integrated control theory of vehicle handling stability will be further improved, and the theoretical fundamentals of nonlinear vehicle dynamics will be provided for the longitudinal and lateral coupled control of intelligent vehicles under extreme conditions (mostly steering and braking working conditions) [23–25].

The content of this paper is arranged as follows: Section 2 is the establishment of a 5DOF steering and braking stability analysis model, and the correctness and effectiveness of the model are verified by simulation analysis. In Section 3, the D'Alembert principle is introduced, and the original model is transformed into an equivalent equilibrium system to analyze the bifurcation of the equilibrium point. In Section 4, the two-dimensional bifurcation parameters set under steering and braking condition are solved by using the equilibrium bifurcation method, and the three-dimensional stability region is fitted. In Section 5, the stable regions of the original system and the equivalent equilibrium system are calculated by the energy dissipation method, and the results are compared with those of the equilibrium bifurcation method. Section 6 gives the conclusions.

2. Stability Analysis of 5DOF Steering and Braking Vehicle Model

2.1. Vehicle Model

To study the stability of the plane motion of vehicles, this paper does not consider the influence of suspension systems and load transfers in steering and braking conditions, that is, the vertical, pitch, and roll motions of vehicles are ignored.

This paper mainly analyzes and calculates the dynamic stability region under vehicle braking. If a double-track model is used, the degrees of freedom of the system model will reach seven. Through previous research, we have found that as the degrees of freedom of the system model increases, the difficulty of accurately solving the equilibrium point greatly increases. Moreover, the dynamic situation in this study can also be effectively analyzed through a 5DOF model. In addition, for front wheel steering vehicles, although the actual steering angles of the two tires are different due to the differential (usually the inner tire has a larger steering angle), this is not the focus of this study. We simplify the double-track model to the single-track model, which can better study how changes in steering angles affect the dynamic mechanism of vehicle steering and braking.

Based on the classical 3DOF steering model [11], the longitudinal force and braking torque of the tires are introduced. The schematic diagrams of the single-track model considering the longitudinal force of the tire and the wheel with braking torque are shown in Figure 1.

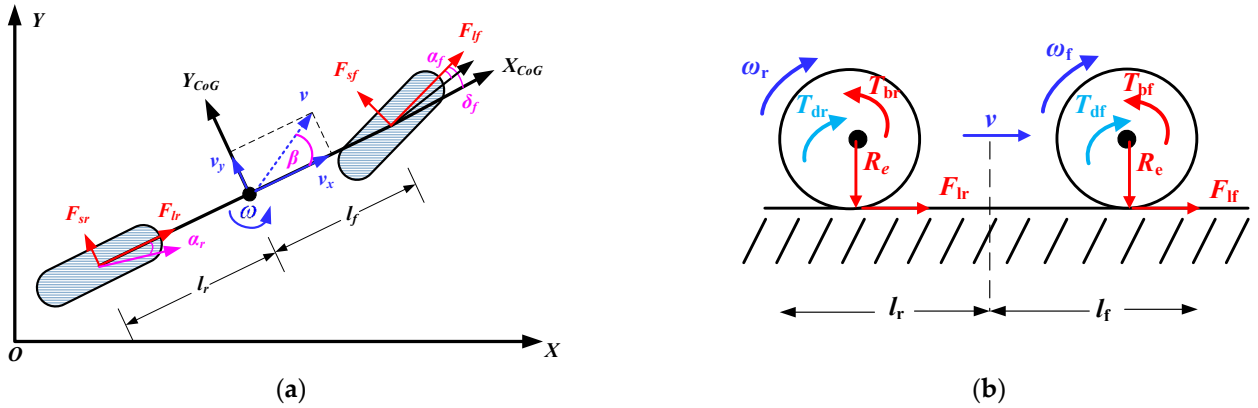

Figure 1. The 5DOF model: (**a**) Single-track model with longitudinal force added; (**b**) The front and rear wheel braking model.

Where X_{CoG} and Y_{CoG} represent the X-axis and Y-axis of the vehicle coordinate system, and X and Y represent the X-axis and Y-axis of the geodetic coordinate system.

When the vehicle velocity is low, the air resistance is small, and the wheel rolling resistance is the main driving resistance. While the vehicle is in high-velocity conditions, air resistance surpasses wheel rolling resistance and becomes the main resistance [26]. The direction of air resistance is always opposite to the driving direction, so it is necessary to introduce symbolic functions into the model to describe the longitudinal and lateral air resistance of the vehicle body. Finally, the 5DOF dynamic system equation can be given as follows:

$$\begin{cases} \dot{v_y} = -v_x\omega + \frac{F_{lf}\sin\delta_f + F_{sf}\cos\delta_f + F_{sr} - \mathrm{sgn}(v_y)\cdot C_{\mathrm{air\_}y}A_{\mathrm{L\_}y}\frac{\rho}{2}v_y^2}{m} \\ \dot{\omega} = \frac{(F_{lf}\sin\delta_f + F_{sf}\cos\delta_f)l_f - F_{sr}l_r}{I_z} \\ \dot{v_x} = v_y\omega + \frac{F_{lf}\cos\delta_f - F_{sf}\sin\delta_f + F_{lr} - \mathrm{sgn}(v_x)\cdot C_{\mathrm{air\_}x}A_{\mathrm{L\_}x}\frac{\rho}{2}v_x^2}{m} \\ \dot{\omega_f} = \frac{-\mathrm{sgn}(\omega_f)\cdot T_{bf} - R_e\cdot F_{lf}}{J} \\ \dot{\omega_r} = \frac{-\mathrm{sgn}(\omega_r)\cdot T_{br} - R_e\cdot F_{lr}}{J} \end{cases} \quad (1)$$

where m is the mass of the vehicle, I_z is the yaw moment of inertia of the vehicle, v_x is the longitudinal velocity, v_y is the lateral velocity, ω is the yaw rate, ω_f is the angular velocity of the front wheels, ω_r is the angular velocity of the rear wheels, l_f is the distance from the front axle to the mass center, l_r is the distance from the rear axle to the mass center, J is the yaw moment of inertia of the wheels, δ_f is the front wheels' steering angle, $C_{\mathrm{air\_}x}$ is the longitudinal air resistance coefficient, $C_{\mathrm{air\_}y}$ is the lateral air resistance coefficient, $A_{\mathrm{L\_}x}$ is the longitudinal area of the vehicle, $A_{\mathrm{L\_}y}$ is the lateral area of the vehicle, ρ is the density of air, T_{bf} is the braking torque of the front wheels, T_{br} is the braking torque of the rear wheels, R_e is the rolling radius of the wheels, F_{lf} and F_{lr} are the longitudinal tire forces of the front wheel and the rear wheel, respectively, and F_{sf} and F_{sr} are the lateral tire forces of the front wheel and the rear wheel, respectively.

For the convenience of description, the braking torque T_b is regarded as a positive scalar in this paper. It is mainly applied to the front wheel to prevent the rear wheel from locking and slipping first. The braking torque of the front and rear wheels is distributed according to the following formula:

$$\begin{cases} T_{bf} = \eta T_b \\ T_{br} = (1-\eta)T_b \end{cases} \quad (2)$$

where η is the braking torque distribution coefficient, and η = 0.7.

To improve the stability of braking and make the best use of the road adhesion conditions, a braking mode with both the front and rear wheels locked simultaneously is adopted. On any road surface with an adhesion coefficient μ (μ = 0.3 in this paper), the

condition for both the front and rear wheels to lock at the same time is that the sum of the braking forces of the front and rear wheels are equal to the adhesion force, and the braking forces of the front and rear wheels are equal to their respective adhesion forces [27], that is:

$$\begin{cases} F_{\mu f} + F_{\mu r} = \mu F_z \\ F_{\mu f} = \mu F_{zf} \\ F_{\mu r} = \mu F_{zr} \end{cases} \tag{3}$$

where $F_{\mu f}$ is the braking force of the front wheel brake, $F_{\mu r}$ is the braking force of the rear wheel brake, and F_z is the total load of the front and rear wheels of the vehicle. Only plane motion is considered, therefore the front wheel load F_{zf} and the rear wheel load F_{zr} are fixed values, and they are distributed as follows:

$$\begin{cases} F_{zf} = \frac{mgl_f}{l_f + l_r} \\ F_{zr} = \frac{mgl_r}{l_f + l_r} \end{cases} \tag{4}$$

Without loss of generality, the simulation in this paper is carried out on a low adhesion coefficient road. The model parameters of the 5DOF system are selected according to [3,28], as shown in Table 1.

Table 1. Vehicle model parameters.

Component Names and Parameters	Values
vehicle mass m/kg	1500
yaw moment of inertia I_z/kg·m^2	3000
the distance from the front axle to the mass center l_f/m	1.2
the distance from the rear axle to the mass center l_r/m	1.3
yaw moment of inertia of the wheels J/kg·m^2	2.0
longitudinal air resistance coefficient $C_{\mathrm{air\_}x}$	0.3
the lateral air resistance coefficient $C_{\mathrm{air\_}y}$	0.4
the longitudinal area of the vehicle $A_{\mathrm{L\_}x}$/m^2	1.7
the lateral area of the vehicle $A_{\mathrm{L\_}y}$/m^2	3.5
the density of air ρ/kg/m^3	1.2258
the rolling radius of the wheels R_{e}/m	0.224

2.2. Tire Model

To reflect the nonlinear characteristics of tire force, the expression of tire force adopts the classic magic formula [29]:

$$F = \mathrm{D}\sin(\mathrm{Carctan}(\mathrm{B}x - \mathrm{E}(\mathrm{B}x - \mathrm{arctanB}x))) \tag{5}$$

where B, C, D, and E are tire parameters, F is the tire steady-state longitudinal force or lateral force, and x is the longitudinal slip rate or sideslip angle.

The calculation of the slip rate is based on the unified formula considering all tire operating conditions in [13].

$$k = \frac{\omega_w R_e - v_{wx}}{|v_{wx}|} \tag{6}$$

The tire velocity in the tire coordinate system is calculated by coordinate transformation.

$$\begin{cases} v_{xf} = v_x \cos\delta_f + (v_y + \omega l_f)\sin\delta_f \\ v_{xr} = v_x \cos\delta_r + (v_y - \omega l_r)\sin\delta_r \end{cases} \tag{7}$$

$$\begin{cases} v_{yf} = -v_x \sin\delta_f + (v_y + \omega l_f)\cos\delta_f \\ v_{yr} = -v_x \sin\delta_r + (v_y - \omega l_r)\cos\delta_r \end{cases} \tag{8}$$

where v_{xf} is the longitudinal velocity of the front wheel in the tire coordinate system, and v_{xr} is the longitudinal velocity of the rear wheel in the tire coordinate system.

The sideslip angle is calculated by using the unified formula which is suitable for the conditions of a large sideslip angle and reverse wheel rotation [1]:

$$\begin{cases} \alpha_f = \arctan\frac{v_{yf}}{v_{xf}} \cdot \mathrm{sgn}\left(v_{xf}\right) \\ \alpha_r = \arctan\frac{v_{yr}}{v_{xr}} \cdot \mathrm{sgn}(v_{xr}) \end{cases} \tag{9}$$

The combined slip of the tire is analyzed and calculated according to the model proposed by Pacejka [30].

$$\begin{cases} F_{lf} = F_{lf0} \cdot G_x \\ F_{lr} = F_{lr0} \cdot G_x \\ G_x = \cos[\arctan\{B_{g,x}(\alpha) \cdot \alpha\}] \\ B_{g,x}(\alpha) = r_{x,1}\cos[\arctan(r_{x,2} \cdot k)] \\ F_{sf} = F_{sf0} \cdot G_y \\ F_{sr} = F_{sr0} \cdot G_y \\ G_y = \cos[\arctan\{B_{g,x}(k) \cdot k\}] \\ B_{g,y}(k) = r_{y,1}\cos[\arctan(r_{y,2} \cdot \alpha)] \end{cases} \tag{10}$$

where F_{lf0}, F_{lr0}, F_{sf0}, F_{sr0} are the longitudinal forces and lateral forces of the front and rear wheels under a steady state, G_x and G_y are the tire force combined slip correction function, and $r_{x,1}$, $r_{x,2}$, $r_{y,1}$, $r_{y,2}$ are the tire force combined slip correction coefficient. The values of the tire model parameters [30] are shown in Table 2.

Table 2. Tire model parameters.

Tire	Longitudinal Tire Parameters				Lateral Tire Parameters				Longitudinal Combined Slip Coefficients		Lateral Combined Slip Coefficients	
	B	C	D	E	B	C	D	E	$r_{x,1}$	$r_{x,2}$	$r_{y,1}$	$r_{y,2}$
Front	11.275	1.56	2574.8	0.4109	11.275	1.56	2574.7	−1.999	35	40	40	35
Rear	18.631	1.56	1749.6	0.4108	18.631	1.56	1749.7	−1.7908				

2.3. Model Validation

In this section, the effectiveness of the model is verified by the phase space trajectory (v_y-ω-v_x) of different single initial conditions, the time series of state variables, and the change of body attitude. See Table 3 for the initial conditions of specific simulations.

Table 3. Initial conditions.

Initial Conditions	v_x (m/s)	v_y (m/s)	ω (rad/s)	δ_f (rad)	T_b (N·m)
1	30	0.1	0.1	0.010	300
2	30	0.1	0.1	0.015	300
3	30	0.1	0.1	0.015	600

Figure 2 shows the simulation results, with a simulation time of 30 s. The blue line, red line, and black line in Figure 2a represent the dynamic behavior of the system under the input of initial conditions 1, 2, and 3, respectively. Under the input of initial condition 1, the phase space trajectory first appears a wide range of semi-circular motion, corresponding to the fluctuation of lateral velocity and yaw rate in Figure 2c for the first 5 s. After that, the phase trajectory inclines downward, which also corresponds to the rapid convergence of lateral velocity and yaw rate in Figure 2c and the linear decrease of longitudinal velocity. It can be seen in Figure 2d from the change of body attitude that the vehicle is in a steady-state steering state and the distance between the two vehicles is decreasing continuously, indicating that the vehicle will eventually be stationary.

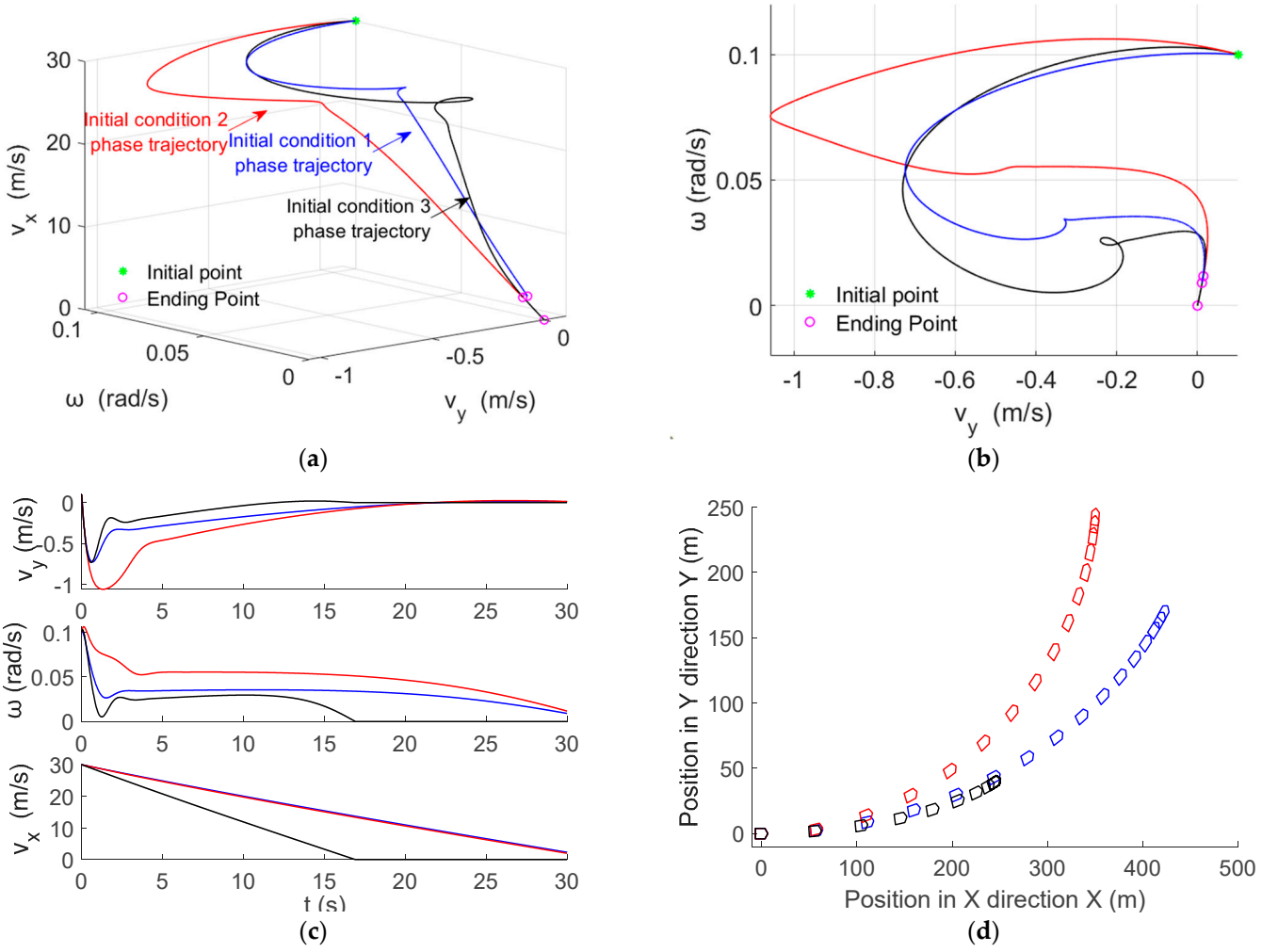

Figure 2. Time-domain responses of single initial conditions and vehicle body attitude: (**a**) Phase space trajectories; (**b**) Top view of a; (**c**) Time-domain responses; (**d**) Vehicle body attitude.

The initial condition 2 increases the front wheel steering angle input compared with the initial condition 1. It can be seen that the motion range of the phase trajectory in the

early stage is larger, and the state variables fluctuate more violently in the early stage as well, but it can still be stabilized. We also can find that the turning radius of the vehicle is smaller than that in the initial condition 1.

The initial condition 3 increases the braking torque input compared with the initial condition 2. It can be seen that the motion range of the phase trajectory in the early stage is smaller, and the fluctuation amplitude of state variables is smaller in the early stage too. The longitudinal velocity linearly decreases to 0 when the simulation time is about 16 s. The vehicle can also be observed to be stationary during the body attitude change, and the overall braking distance is significantly reduced compared with the previous two groups of simulations.

From the above analysis, it can be found that the 5DOF model can reflect the motion process of the vehicle under the combined steering and braking conditions, thus providing a basic analysis model for studying the dynamic bifurcation characteristics of the vehicle under the combined steering and braking conditions.

3. Solution of Equivalent Equilibrium Point

3.1. Introducing the D'Alembert Principle into the 5DOF Model

The vehicle dynamics system is a typical nonlinear system, and the common classical analysis method is the static bifurcation theory based on the change of the number of equilibrium points of the nonlinear system. Many scholars have studied vehicle steering stability. Under the premise of constant longitudinal velocity, the dynamic essence of vehicle steering instability can be attributed to the bifurcation of the equilibrium point in nonlinear dynamics [2,3,5]. However, under the steering and braking conditions, because the longitudinal velocity of the vehicle is constantly changing, there is no equilibrium state according to the strict definition. As a result, the mature research method of steering bifurcation cannot be directly applied to the braking process. Therefore, it is necessary to explore new methods to analyze the bifurcation characteristics of braking.

Horiuchi mentioned in [18] that when analyzing the acceleration or braking of a vehicle system, the virtual force in the D'Alembert principle can be introduced so that an accelerated system can be transformed into an equivalent equilibrium system. The conversion method involves applying a virtual external force determined by acceleration to the system. Based on this principle, if a virtual force with the size of $F = ma$ is applied to the vehicle (where the acceleration is acting on the center of mass of the vehicle), the braking process can be regarded as an equilibrium state (called equivalent equilibrium in this paper) and bifurcation analysis can then be carried out.

Figure 3 gives the force analysis diagram of the whole vehicle after adding the virtual force:

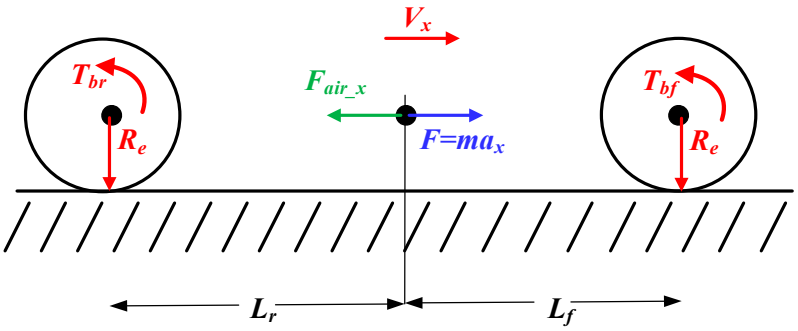

Figure 3. Force analysis diagram with virtual force added.

To maintain the longitudinal force equilibrium of the vehicle, the following can be obtained:

$$ma_x = \frac{T_b}{R_e} + \mathrm{sgn}(v_x) C_{\mathrm{air\_}x} A_{\mathrm{L\_}x} \frac{\rho}{2} v_x^2 \tag{11}$$

The virtual acceleration a_x acting on the center of mass of the vehicle body can be obtained:

$$a_x = \frac{\left(\frac{T_b}{R_e} + \mathrm{sgn}(v_x) C_{\mathrm{air\_}x} A_{\mathrm{L\_}x} \frac{\rho}{2} v_x^2\right)}{m} \tag{12}$$

The equilibrium in the plane motion of the vehicle must satisfy the steady state equation, and it is constructed by making the right side of the dynamic equations equal to zero [31]. The accuracy of the equilibrium point solution is evaluated by the value of the fitness function. That is, the smaller the objective function value, the more accurate the solution. The equation for solving the equivalent equilibrium point of the system is as follows:

$$\begin{cases} \dot{v_y} = -v_x\omega + \frac{F_{lf}\sin\delta_f + F_{sf}\cos\delta_f + F_{sr} - \mathrm{sgn}(v_y)\cdot C_{\mathrm{air\_}y} A_{\mathrm{L\_}y} \frac{\rho}{2} {v_y}^2}{m} = 0 \\ \dot{\omega} = \frac{(F_{lf}\sin\delta_f + F_{sf}\cos\delta_f) l_f - F_{sr} l_r}{I_z} = 0 \\ \dot{v_x} = v_y\omega + \frac{F_{lf}\cos\delta_f - F_{sf}\sin\delta_f + F_{lr} - \mathrm{sgn}(v_x)\cdot C_{\mathrm{air\_}x} A_{\mathrm{L\_}x} \frac{\rho}{2} {v_x}^2 + m a_x}{m} = 0 \\ \dot{\omega_f} = \frac{-\mathrm{sgn}(\omega_f)\cdot T_{bf} - R_e\cdot F_{lf}}{J} = 0 \\ \dot{\omega_r} = \frac{-\mathrm{sgn}(\omega_r)\cdot T_{br} - R_e\cdot F_{lr}}{J} = 0 \end{cases} \tag{13}$$

The equilibrium point solution of a 5DOF system can be regarded as a programming problem constrained by Equation (13):

$$\min f\left(\dot{v}_x, \dot{v}_y, \dot{\omega}, \dot{\omega}_f, \dot{\omega}_r\right) = \left|\dot{v}_x\right| + \left|\dot{v}_y\right| + \left|\dot{\omega}\right| + \left|\dot{\omega}_f\right| + \left|\dot{\omega}_r\right| \tag{14}$$

The optimal solution $\left(\dot{v}_x^*, \dot{v}_y^*, \dot{\omega}^*, \dot{\omega}_f^*, \dot{\omega}_r^*\right)$ must satisfy $f\left(\dot{v}_x^*, \dot{v}_y^*, \dot{\omega}^*, \dot{\omega}_f^*, \dot{\omega}_r^*\right) = 0$, and the fitness value of the 5DOF system is as follows:

$$\mathrm{Fitness} = \left|\dot{v}_x\right| + \left|\dot{v}_y\right| + \left|\dot{\omega}\right| + \left|\dot{\omega}_f\right| + \left|\dot{\omega}_r\right| \tag{15}$$

To verify the equivalent equilibrium state of the nonlinear system after adding the virtual force, Figure 4 shows the comparison of multiple initial point phase trajectory and single initial point state variables time series of the system without or with the virtual force.

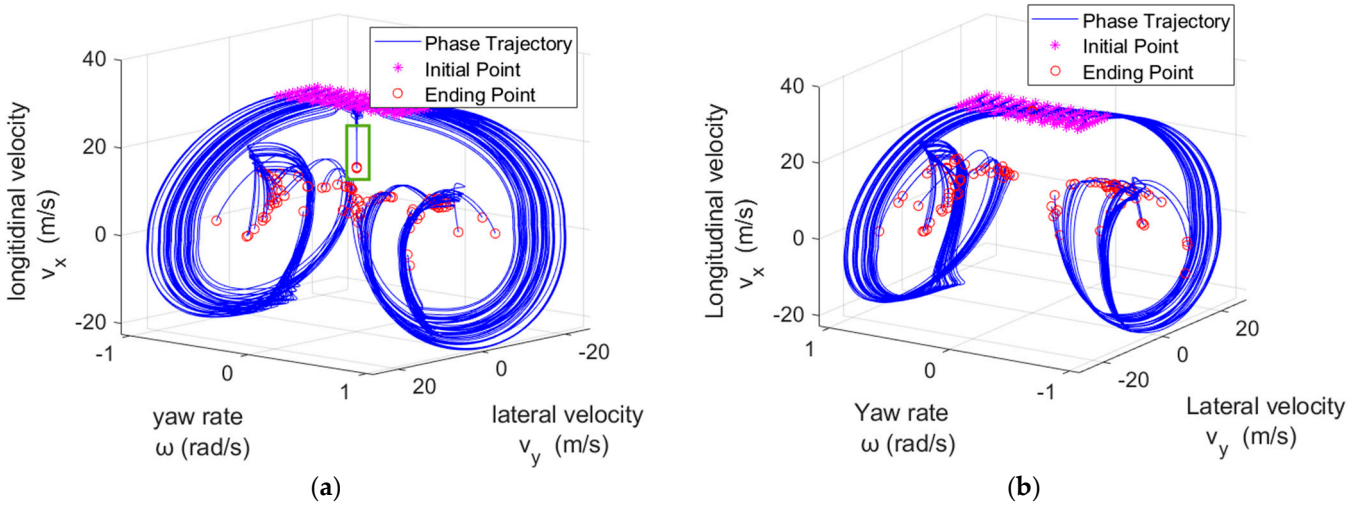

Figure 4. *Cont.*

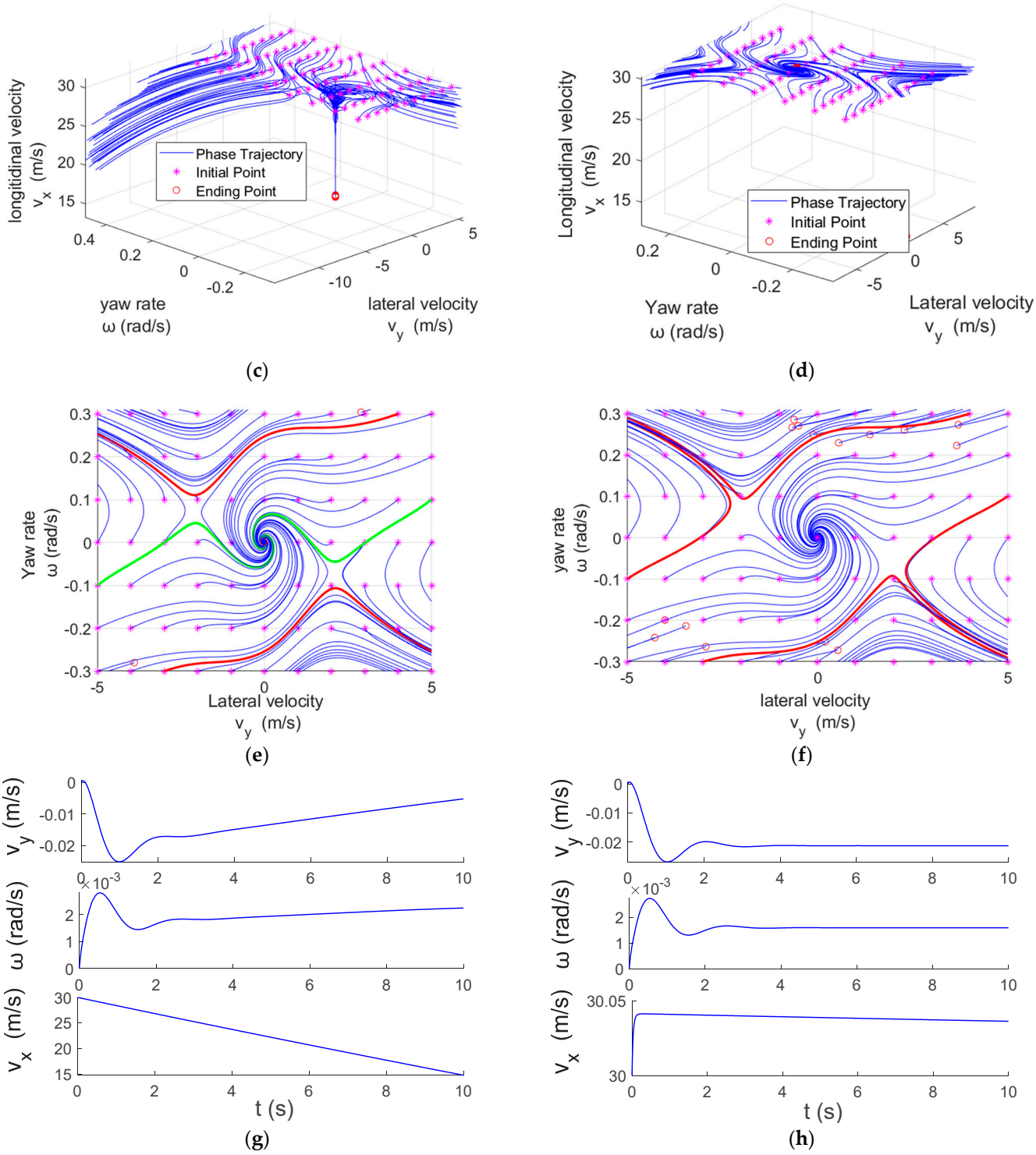

Figure 4. Comparison of the 5DOF model with and without virtual force: (**a**) Phase space without adding virtual force; (**b**) Phase space with virtual force; (**c**) Local view of (**a**); (**d**) Local view of (**b**); (**e**) Phase plane without virtual force; (**f**) Phase plane with virtual force; (**g**) Time domain without virtual force; (**h**) Time domain with virtual force.

The initial conditions of the multi-initial points simulation are: longitudinal velocity v_x = 30 m/s, front wheel steering angle δ_f = 0.001 rad, braking torque T_b = 500 N·m, lateral velocity v_y ranging from −10 m/s to 10 m/s, with intervals of 1 m/s, and the value range of the yaw rate ω is −0.5 rad/s to 0.5 rad/s, with value intervals of 0.1 rad/s. The single initial

point simulation conditions are: longitudinal velocity v_x = 30 m/s, front wheel steering angle δ_f = 0.001 rad, and braking torque T_b = 500 N·m.

Figure 4a,b show the global dynamic characteristics of the system, and it can be seen that the global characteristics of the system have not changed obviously after adding the virtual force. However, by comparing the local diagrams of Figure 4c,d, it can be seen that the downward spiral motion trend of the phase trajectory (phase trajectory in the green rectangle in Figure 4a) disappears and is replaced by the spiral motion in the two-dimensional plane in Figure 4d. This means that the longitudinal velocity of these phase trajectories remains constant.

The attraction domains of Figure 4e,f are almost the same. It is noted that the two green phase trajectories at the edge of the attraction domain in Figure 4f can return to the original point, while they cannot become stable in Figure 4e. It is indicated that the stability of the system is slightly improved.

Figure 4g,h are time series of phase trajectory state variables under stable initial conditions. It can be seen that the longitudinal velocity changes from linear decreasing to basically constant, and the lateral velocity and yaw rate also remain constant during the simulation time. It shows that the system under these initial conditions can achieve the equivalent equilibrium state. Figure 4 confirms the equivalent equilibrium state of the system from the global and local perspectives, so that the static bifurcation analysis of the nonlinear system can be carried out.

3.2. Analysis of Bifurcation Characteristics of Equilibrium Point

In this section, the equilibrium point of the vehicle dynamics equivalent system is solved by an improved hybrid algorithm based on the genetic algorithm (GA) and sequential quadratic programming (SQP) method [32]. The specific solution flow chart is shown in Figure 5.

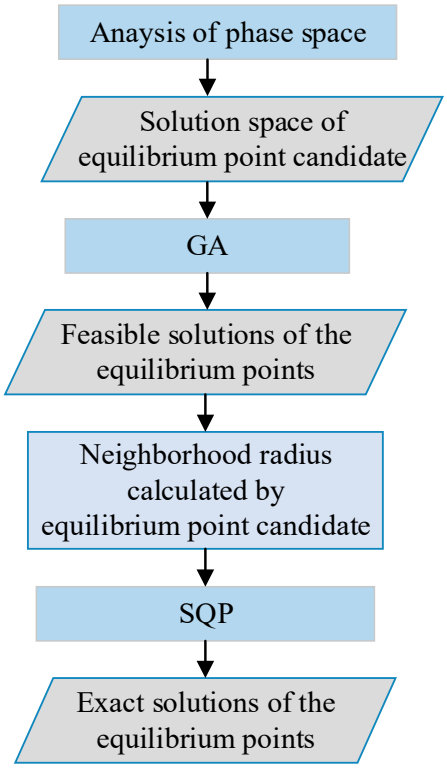

Figure 5. The hybrid solving process.

The solution conditions are: initial longitudinal velocity v_x = 30 m/s, front wheel angle δ_f = 0.015 rad, and the search range of braking torque T_b is [0, 504] N·m, with value intervals

of 10.08 N·m (the bifurcation of the equilibrium point is solved to the order of 0.01 N·m). According to the solution process of the equilibrium point in Figure 5, the corresponding virtual acceleration a_x is calculated under each given braking torque T_b, and the equivalent equilibrium state is constructed so as to complete the solution of the equilibrium point.

Figure 6 shows the bifurcation diagram of the equilibrium point with braking torque as the bifurcation parameter. Tables 4–6 show the partial values of the stable equilibrium point and two unstable equilibrium points of the system when the braking torque changes.

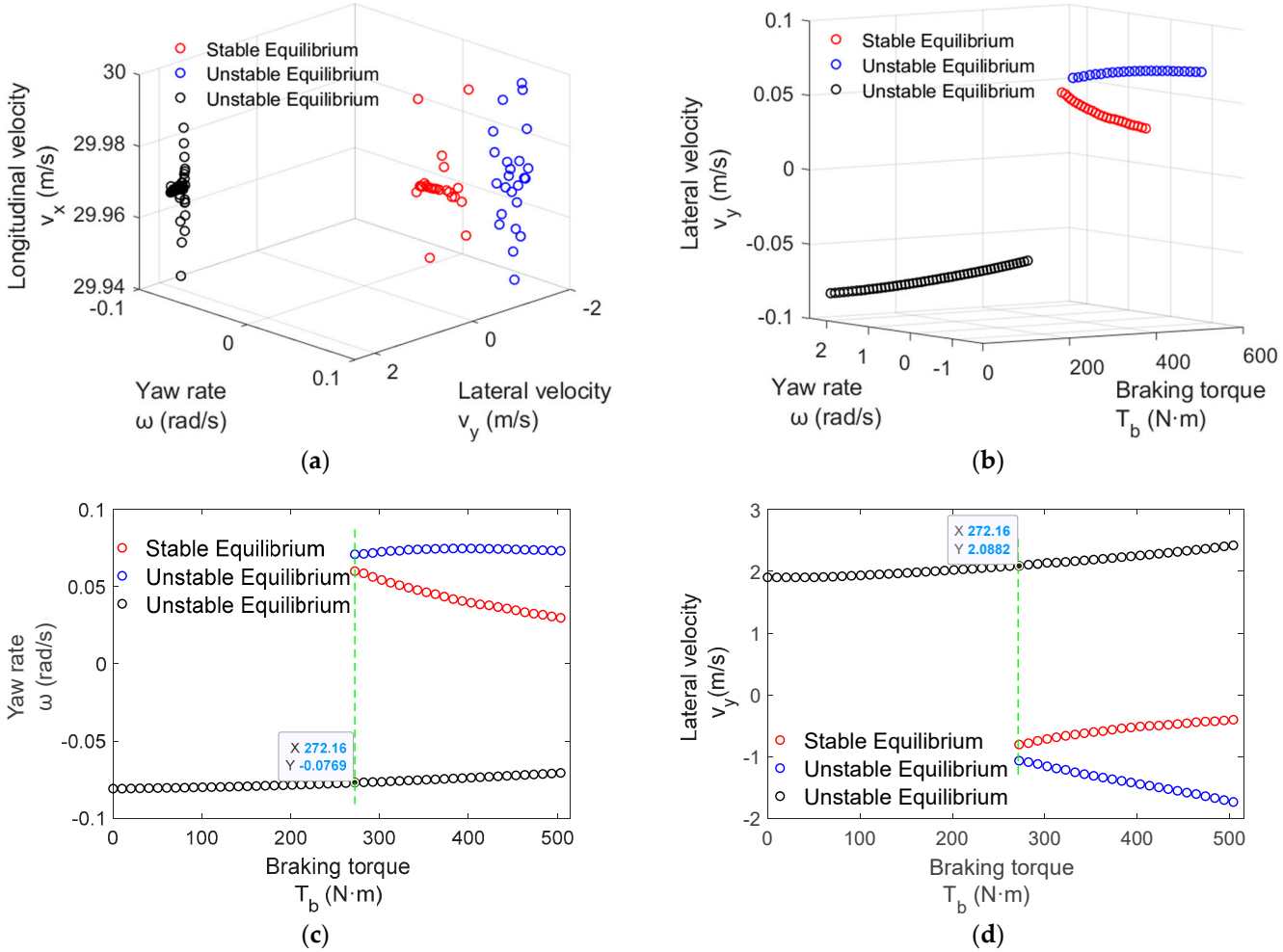

Figure 6. Range of the equilibrium points and bifurcation diagram of equilibrium points with braking torque varying: (**a**) Spatial distribution of equilibrium points; (**b**) Bifurcation space of the equilibrium points; (**c**) Bifurcation diagram of equilibrium points; (**d**) Bifurcation diagram of equilibrium points.

Table 4. Vehicle dynamics partial values for stable equilibrium points.

T_b (N·m)	Vehicle Dynamics Equilibriums					Rate of System Variable Change					Fitness
	v_y (m/s)	ω (rad/s)	v_x (m/s)	ω_f (rad/s)	ω_r (rad/s)	$\dot{v}_y$	$\dot{\omega}$	$\dot{v}_x$	$\dot{\omega}_f$	$\dot{\omega}_r$	
272.16	−0.8008	0.0600	29.9973	132.3378	132.5518	0.0000	0.0023	−0.0621	0.0001	0.0000	0.0646
322.56	−0.6604	0.0509	29.9670	129.5839	132.2900	0.0000	0.0000	−0.0452	0.0000	0.0000	0.0452
372.96	−0.5614	0.0435	29.9687	129.0988	132.1528	0.0000	0.0012	−0.0343	0.0004	0.0000	0.0359
423.36	−0.4939	0.0379	29.9494	128.4523	131.9026	0.0000	0.0000	−0.0270	0.0000	0.0000	0.0271
473.76	−0.4302	0.0325	29.9691	127.9211	131.8235	0.0000	0.0009	−0.0213	0.0000	0.0000	0.0222

Table 5. Vehicle dynamics partial values for one unstable equilibrium point.

T_b (N·m)	Vehicle Dynamics Equilibriums					Rate of System Variable Change					Fitness
	v_y (m/s)	ω (rad/s)	v_x (m/s)	ω_f (rad/s)	ω_r (rad/s)	$\dot{v}_y$	$\dot{\omega}$	$\dot{v}_x$	$\dot{\omega}_f$	$\dot{\omega}_r$	
272.16	−1.0630	0.0709	29.9855	129.7561	132.2881	0.0000	0.0037	−0.0919	0.0000	0.0000	0.0956
322.56	−1.2107	0.0732	29.9939	128.9161	131.9043	0.0000	−0.0014	−0.1057	0.0000	0.0000	0.1071
372.96	−1.3626	0.0746	29.9676	127.8544	131.3307	0.0000	0.0001	−0.1188	0.0000	0.0000	0.1188
423.36	−1.4954	0.0745	29.9688	126.8547	130.8688	0.0000	0.0000	−0.1286	0.0000	0.0000	0.1286
473.76	−1.6361	0.0738	29.9702	125.7211	130.3674	0.0000	0.0000	−0.1378	0.0000	0.0000	0.1378

Table 6. Vehicle dynamics partial values for another unstable equilibrium point.

T_b (N·m)	Vehicle Dynamics Equilibriums					Rate of System Variable Change					Fitness
	v_y (m/s)	ω (rad/s)	v_x (m/s)	ω_f (rad/s)	ω_r (rad/s)	$\dot{v}_y$	$\dot{\omega}$	$\dot{v}_x$	$\dot{\omega}_f$	$\dot{\omega}_r$	
60.48	1.9081	−0.0804	29.9688	132.8727	133.2487	0.0000	0.0000	−0.1343	0.0000	−0.0001	0.1345
120.96	1.9501	−0.0798	29.9851	131.9924	132.7804	0.0000	0.0000	−0.1367	0.0001	0.0000	0.1368
181.44	2.0027	−0.0789	29.9691	131.0290	132.1721	0.0000	0.0000	−0.1392	0.0000	0.0000	0.1392
241.92	2.0624	−0.0777	29.9596	130.1154	131.5962	0.0000	0.0000	−0.1414	0.0000	0.0001	0.1418
302.40	2.1372	−0.0765	29.9692	129.2572	131.0944	0.0000	−0.0030	−0.1452	0.0000	0.0000	0.1483
362.88	2.2020	−0.0749	29.9694	128.3242	130.5514	0.0000	0.0000	−0.1471	0.0000	0.0000	0.1471
423.36	2.2848	−0.0732	29.9698	127.2831	129.9736	0.0000	0.0000	−0.1499	0.0001	0.0000	0.1500
483.84	2.3826	−0.0714	29.9698	126.0794	129.3452	0.0000	0.0000	−0.1532	0.0000	0.0000	0.1532

Figure 6a shows the variation of values of all equilibrium points obtained by the hybrid algorithm. It can be seen that the longitudinal velocity v_x of the equilibrium points is around 30 m/s. Figure 6 shows the bifurcation diagrams of equilibrium points from different perspectives, with red "○" indicating stable equilibrium points, and blue and black "○" indicating unstable equilibrium points.

Through the analysis of the equivalent equilibrium point of the system, it can be concluded that when the value of the braking torque T_b is less than 272.16 N·m, there is only one unstable equilibrium point in the system. As the braking torque increases, the closer the system approaches the stable equilibrium point, the easier it is to stabilize. When the value of braking torque T_b exceeds 272.16 N·m, another unstable equilibrium point and stable equilibrium point of the system appear.

Based on the above analysis, it can be confirmed that the change in the number of equilibrium points of system with the change of braking torque T_b is a typical static bifurcation phenomenon. For this phenomenon, we can visually observe the change in the number of equilibrium points through the phase plane diagram, as shown in Figure 7. The initial conditions for the multi-initial points simulation are: longitudinal velocity v_x = 30 m/s, front wheel steering angle δ_f = 0.015 rad, lateral velocity range of −5 m/s to 5 m/s, with intervals of 1 m/s, and range of yaw rate values ω from −0.5 rad/s to 0.5 rad/s, with intervals of 0.2 rad/s.

When the braking torque is T_b = 262.08 N·m, as shown in Figure 7a, the system only has one unstable saddle point (which can be confirmed as a saddle point based on the phase trajectory manifold around the equilibrium point), and from the phase trajectories in the lower left corner, it can be seen that the phase trajectories in the area are connected. When the braking torque T_b = 272.16 N·m, the phase trajectory in the small graph in the lower left corner separates, resulting in the stable focus point and another unstable saddle point. The change in the number of equilibrium points before and after the increase of braking torque indicates that the system has undergone static bifurcation, which is consistent with the equilibrium point bifurcation diagram in Figure 7.

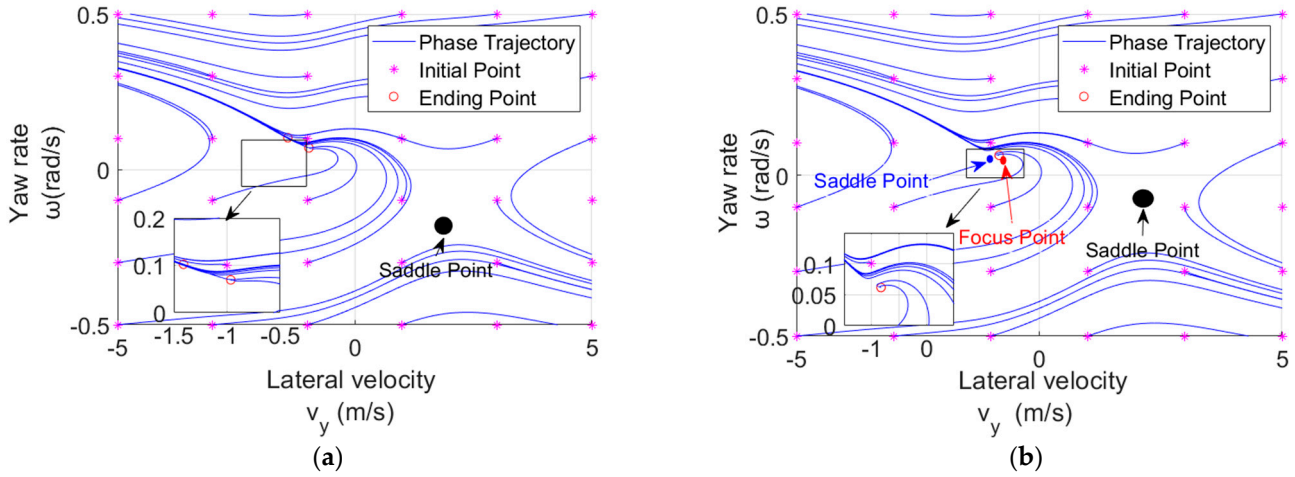

Figure 7. Change of phase plane before and after bifurcation: (**a**) T_b = 262.08 N·m; (**b**) T_b = 272.16 N·m.

4. Solution of Stability Region

4.1. Solution Procedure

Based on the previous achievements of our research team [14] in driving steering stability regions, the idea of constructing a two-dimensional bifurcation parameter set using system input parameters (front wheel angle-braking torque) will be applied again. The specific solution flow is shown in Figure 8, and the specific solving steps are as follows:

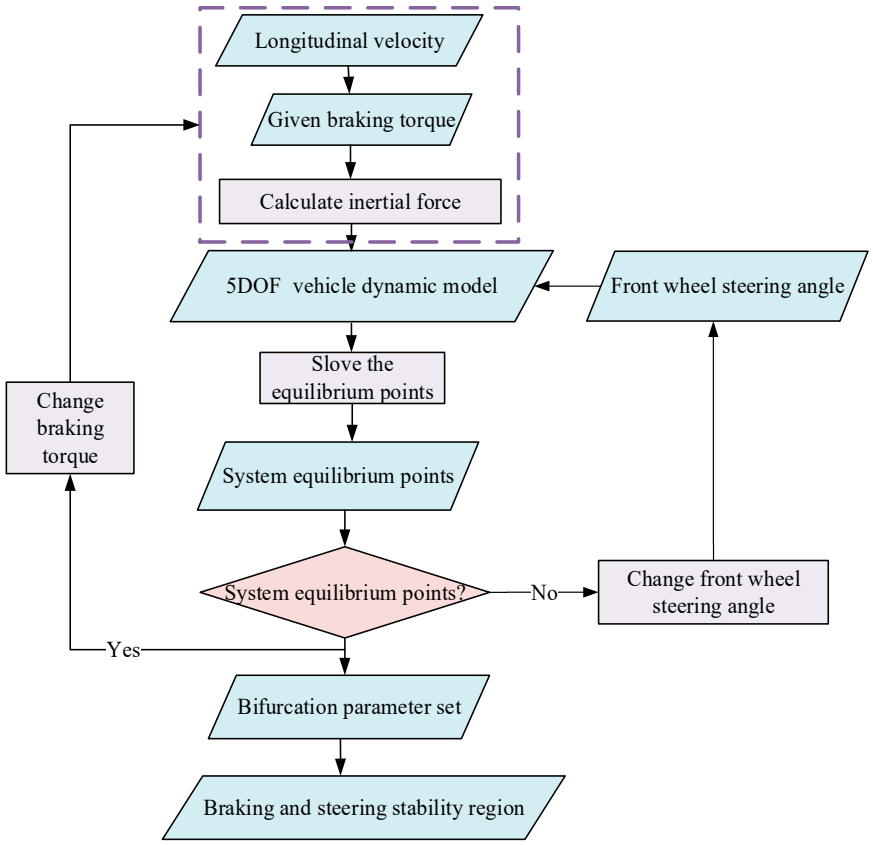

Figure 8. Flow chart for determining the steering and braking stability region.

Step 1. The initial longitudinal velocity range is 10 m/s to 60 m/s, with step sizes of 10 m/s.

Step 2. The initial braking torque is 10.08 N·m and is then continuously increased according to the given step size (the braking torque step size is 10.08 N·m) in each cycle until 604 N·m. After applying the braking torque each time, the corresponding inertia acceleration is calculated through Equation (12).

Step 3. The equilibrium points of the 5DOF equivalent system are solved and it is determined whether it is equilibrium point bifurcation according to the definition of static bifurcation. If so, the front wheel steering angle value of the bifurcation point is recorded and the braking torque is increased to continue solving the system equivalent equilibrium point; if not, searching for the front wheel steering angle value of the bifurcation point when the number of equilibrium points changes continues.

Step 4, The two-dimensional bifurcation parameter set (front wheel steering angle-braking torque) for a given initial longitudinal velocity is obtained.

4.2. Fitting of Three-Dimensional Stable Region

Figure 9 shows the two-dimensional bifurcation parameter set composed of the front wheel steering angle and braking torque at the given velocity, which is the boundary of the steering and braking stability region. In other words, within this boundary the system is stable.

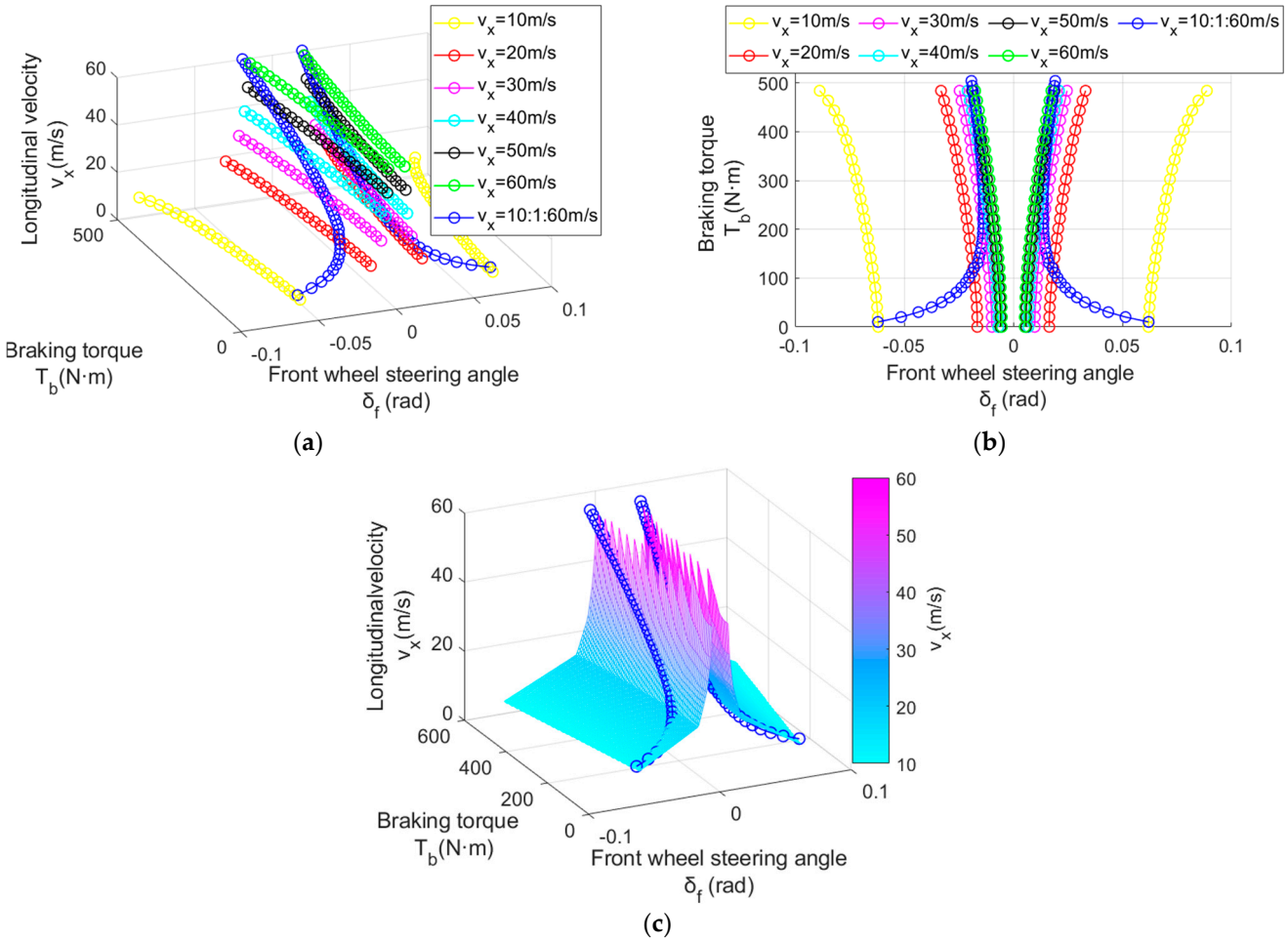

Figure 9. Steering and braking stability region: (**a**) Bifurcation parameter set in δ_f-T_b-v_x space; (**b**) Bifurcation parameter set in the δ_f-T_b plane; (**c**) Steering and braking stability region and surface fitting.

It can be observed in Figure 9a,b that the boundary of the stability region is a hyperbola. With the increase in velocity, the stability region gradually decreases. Especially, when the

longitudinal velocity v_x = 10 m/s increases to v_x = 20 m/s, the stability region is significantly reduced. When the longitudinal velocity v_x = 50 m/s increases to v_x = 60 m/s, the stability region does not change much and only shrinks slightly. The blue circle line is a set of two-dimensional bifurcation parameters solved at different velocities. It can be seen that it passes through the boundary of the stability region at a given velocity in three-dimensional space, thereby mutually proving the correctness of the solved data.

Figure 9b shows the relationship between the bifurcation parameters at a given initial velocity and different initial velocities: when the initial velocity is the same, as the braking torque increases, the front wheel steering angle at the bifurcation point gradually increases; when the initial velocity continues to increase, as the braking torque increases, the front wheel angle at the bifurcation point gradually decreases, but then gradually increases after decreasing to a certain extent.

When there is more and more data on the two-dimensional bifurcation parameter set, theoretically, the steering and braking stability region should be composed of two symmetrical two-dimensional surfaces and a three-dimensional coordinate system. Figure 9c is a hyperboloid (three-dimensional parameter space) fitted according to six sets of boundary data of the stable region from v_x = 10 m/s to v_x = 60 m/s, that is, the boundary surface of the stable region. The surface interpolation method adopts the default "linear" method of MATLAB 2022a. The blue circle line in Figure 9 crosses the curved surface obliquely, which also proves the correctness of the fitted hyperboloid.

5. Verification Based on the Energy Dissipation Method

5.1. Analysis of Energy Dissipation Process

During the braking process of vehicles, tire force and air resistance can cause a decrease in system energy. By analyzing the energy dissipation of the steering and braking conditions of the vehicle, the stability region with and without inertia force applied at a given initial longitudinal velocity is calculated. A comparative analysis is also conducted with the stability region obtained from the equilibrium point bifurcation method in Section 4.2.

The energy dissipation process of a vehicle system can be divided into two parts as shown in Figure 10:

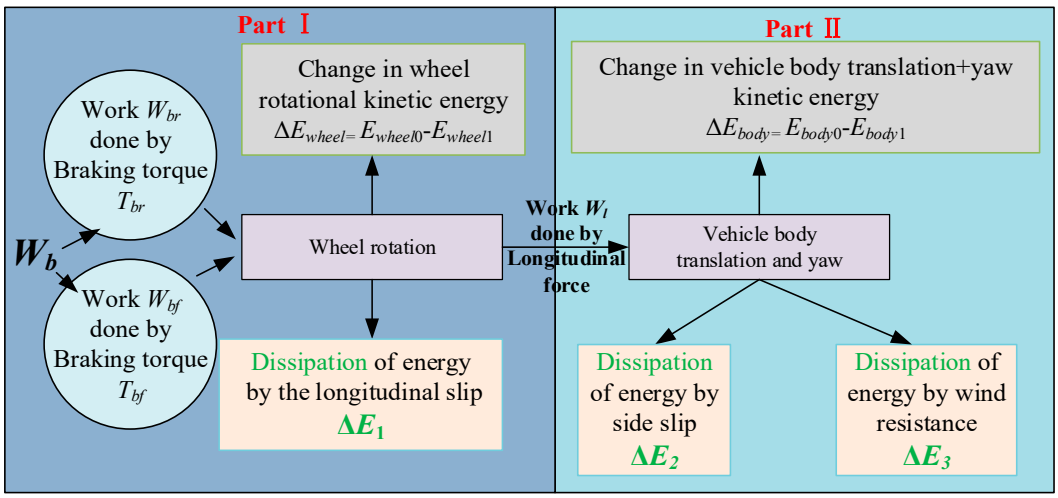

Figure 10. Schematic diagram of the energy dissipation process of the 5DOF vehicle system.

The first part is the dissipation of wheel rotational energy caused by tire longitudinal slip ΔE_1. As soon as the braking torque is applied to the front and rear wheels, the tire and ground experience longitudinal slip. The resulting longitudinal force reacts on the wheel to hinder the vehicle from moving forward. At this time, the effect of the braking torque causes a decrease in the rotational kinetic energy E_{wheel} of the wheel itself.

The second part is the energy dissipation caused by the lateral force generated by the cornering characteristics between the tire and the ground, ΔE_2, and the energy dissipation caused by the air resistance, ΔE_3. The lateral force of the tire and the air resistance act on the vehicle together, causing a change in the sum of the lateral translational kinetic energy and yaw kinetic energy of the body, E_{body}.

Based on the above analysis and energy conversion principle, there is:

$$W_b + \Delta E_1 + \Delta E_2 + \Delta E_3 = \left(E_{\text{wheel}_1} + E_{\text{body}_1}\right) - \left(E_{\text{wheel}_0} + E_{\text{body}_0}\right) \tag{16}$$

In Equation (16), w_b is the work done by the braking torque, E_{wheel0} is the rotational kinetic energy of the vehicle body at the initial simulation time, E_{wheel1} is the rotational kinetic energy of the vehicle body at the end of the simulation time, E_{body0} is the sum of the lateral translational kinetic energy and yaw kinetic energy of the vehicle body at the initial simulation time, and E_{body1} is the sum of the lateral translational kinetic energy and yaw kinetic energy of the vehicle body at the end of the simulation time.

The total dissipated energy ΔE of the 5DOF model can be calculated as:

$$\begin{aligned} \Delta E &= \Delta E_1 + \Delta E_2 + \Delta E_3 \\ &= \left(E_{\text{wheel}_1} + E_{\text{body}_1}\right) - \left(E_{\text{wheel}_0} + E_{\text{body}_0}\right) - W_b \end{aligned} \tag{17}$$

To facilitate the display of calculation results, the calculation of dissipated energy is taken as a positive value, and the calculation expression of dissipated energy is further refined as follows:

$$\begin{aligned} &\Delta E = W_b + \left(E_{\text{wheel}_0} + E_{\text{body}_0}\right) - \left(E_{\text{wheel}_1} + E_{\text{body}_1}\right) = \int_{t0}^{t1} (T_{bf} \cdot \omega_f + T_{br} \cdot \omega_r) dt \\ &+ (\tfrac{1}{2} m {v_{x0}}^2 + \tfrac{1}{2} m {v_{y0}}^2 + \tfrac{1}{2} {\omega_0}^2 {I_z}^2 + \tfrac{1}{2} J {\omega_{f0}}^2 + \tfrac{1}{2} J {\omega_{r0}}^2) - \\ &(\tfrac{1}{2} m {v_{x1}}^2 + \tfrac{1}{2} m {v_{y1}}^2 + \tfrac{1}{2} {\omega_1}^2 {I_z}^2 + \tfrac{1}{2} J {\omega_{f1}}^2 + \tfrac{1}{2} J {\omega_{r1}}^2) \end{aligned} \tag{18}$$

where ω_f and ω_r are the angular velocities of the front and rear wheels, v_{x0}, v_{y0}, ω_0, ω_{f0} and ω_{r0} are longitudinal velocity, lateral velocity, yaw rate, and front and rear wheel angular velocities at the initial simulation time, and v_{x1}, v_{y1}, ω_1, ω_{f1} and ω_{r1} are longitudinal velocity, lateral velocity, yaw rate, and front and rear wheel angular velocity at the end of the simulation.

5.2. Comparison and Verification

Figure 11 provides both the energy dissipation diagram and projection diagram of the system with the inertia force applied. The initial longitudinal velocities are v_x = 30 m/s and v_x = 50 m/s, respectively. The ranges of δ_f are −0.03 rad to 0.03 rad and −0.02 rad to 0.02 rad, with step sizes of 0.0005 rad. The range of T_b is 0 to 504 N·m, with step sizes of 10.08 N·m.

Figure 11a,c show that the energy dissipation results of the system at two initial velocities have positive and negative values, and the energy dissipation increases with the increase of velocity. The occurrence of negative values is due to the increase of energy caused by the positive work of the inertia force. However, it does not affect the hierarchical distribution trend of energy. The blue part in Figure 11 has a lower energy dissipation, resembling a trapezoid, and is the stable region for the steering and braking condition. The purple part has a high energy dissipation and smooth surface distribution trend, which represents the unstable region of the steering and braking condition.

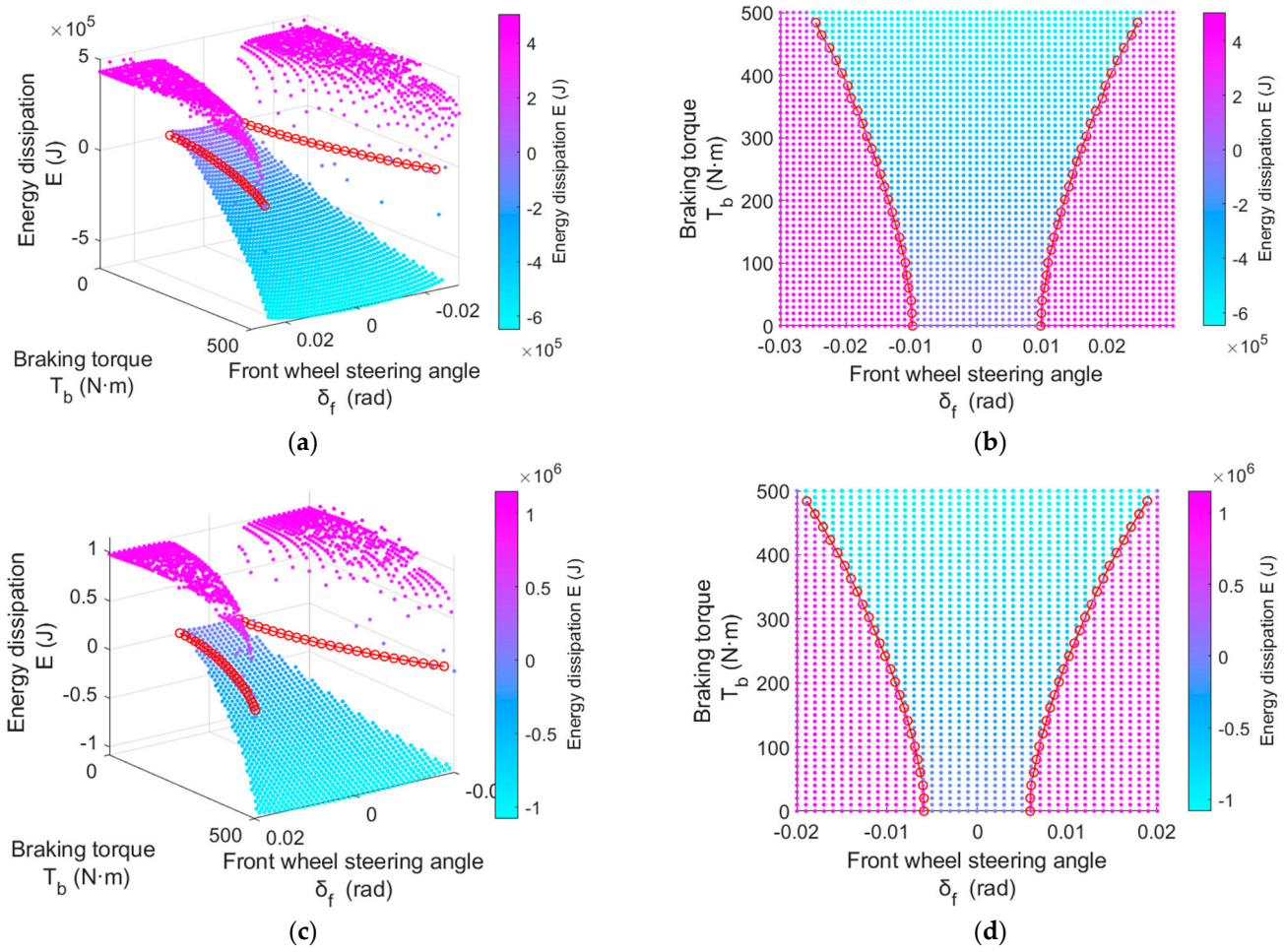

Figure 11. Steering and braking stability region with virtual force: (**a**) v_x = 30 m/s; (**b**) top view of (**a**); (**c**) v_x = 50 m/s; (**d**) top view of (**c**).

Figure 11b,d compare the boundary lines of the stability region obtained by the energy dissipation method (the boundary lines of the purple and blue parts) with the boundary lines obtained by the bifurcation method (the red circle line). It can be seen that both of them are almost identical. Furthermore, taking Figure 11d as an example, we can observe some quantitative phenomena. When limiting the front wheel steering angle or braking torque, we can easily see the range of stability and instability of the system. For example, when the braking torque is limited to 100 N·m, the area where the absolute value of the front wheel angle is greater than 0.006 rad is the instability region, and the area less than 0.006 rad is the stability region. When the front wheel steering angle is limited to 0.01 rad and the braking torque is greater than 231.84 N·m, it is considered a stable region, and, vice versa, it is considered an unstable region.

In order to study the stability region under steering and braking conditions using the classical bifurcation analysis method, the virtual force is applied for converting the original model into an equivalent system. However, due to the difference of dynamic characteristics between the equivalent system and the original system after the addition of the virtual force, the energy dissipation method is used to calculate the steering and braking stability region of the original system.

Figure 12 provides the schematic diagram and projection of the energy dissipation of the system without applying virtual force, which is also compared with the stability region obtained by the equilibrium point bifurcation method.

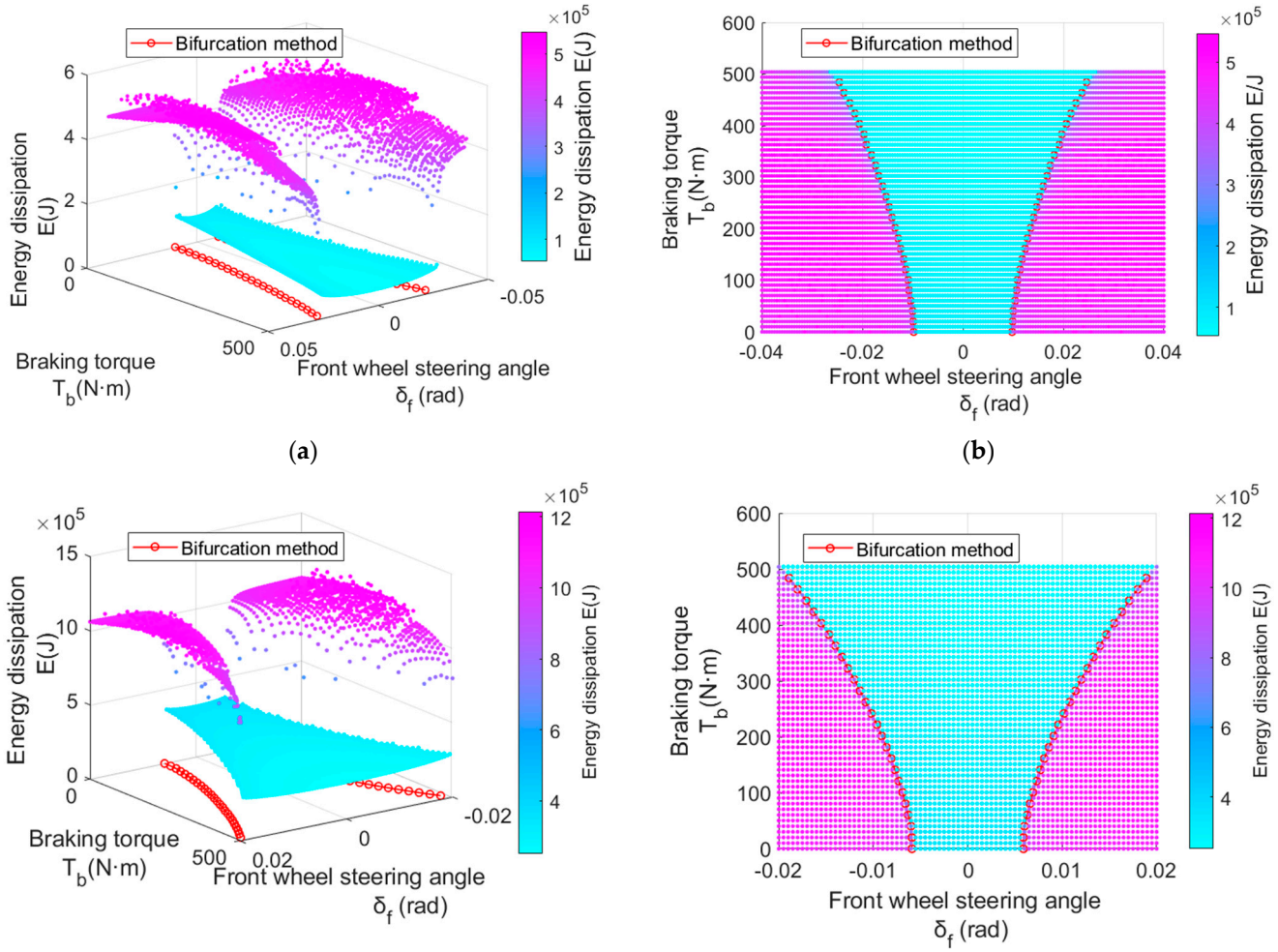

Figure 12. Steering and braking stability region without virtual force: (**a**) v_x = 30 m/s; (**b**) top view of (**a**); (**c**) v_x = 50 m/s; (**d**) top view of (**c**).

From Figure 12, it can be seen that there is no external input of virtual force on the system, and the energy dissipation is all positive, showing a clear layered distribution. The blue part has a lower energy dissipation, resembling a trapezoid, which is the stable region for the steering and braking condition. The purple part has a high energy dissipation and smooth surface distribution trend, which represents the unstable region of the steering and braking condition.

The boundary of the energy dissipation stable region can be seen in Figure 12 (the boundary lines of the purple energy region and the blue energy region are clearer than those of the system with added inertia force). At the same time, they are compared with the boundary obtained by the bifurcation method. It can be seen that when v_x = 30 m/s and v_x = 50 m/s, the results show that the stability regions of the 5DOF system with and without the application of virtual force almost remain the same. From Figure 12b,d, it can be seen that when the braking torque is limited to 500 N·m and the initial longitudinal velocity is 30 m/s, the absolute value of the front wheel steering angle at the boundary point is greater than 0.02 rad. When the initial longitudinal velocity increases to 50 m/s, the absolute value of the front wheel angle at the boundary point is less than 0.02 rad. This means that as the vehicle velocity increases, the stable region shrinks.

Compared with traditional equilibrium point bifurcation based stability region solving methods, the energy dissipation method based stability region verification method has better solving efficiency. The equilibrium point bifurcation method determines the

bifurcation point through phase trajectory. It takes approximately 5.12 s to calculate one bifurcation point in MATLAB. Assuming that the solving speed of all bifurcation points is basically the same and taking Figure 12d as an example, there are a total of 50 bifurcation points in Figure 12d and the total solution time is approximately 241.5 s. In addition, it also takes a lot of data processing time. The time required to solve the stability region using the energy dissipation method is approximately 200.668 s. All the simulations were conducted on a hardware device with an Intel i5-10210U CPU.

6. Conclusions

In this paper, the stability region of the steering and braking condition in vehicle planar motion is solved by the equilibrium point bifurcation analysis method. In addition, it is verified using the energy dissipation method. The main work and conclusions are as follows:

(1) A 5DOF vehicle dynamic model has been established that can analyze the stability of vehicles under steering and braking conditions effectively. The application conditions of braking torque, the locking of front and rear wheels, and the limitation of road adhesion are considered in the model. The validation results indicate that this model can describe the dynamic characteristics of vehicle braking and steering conditions accurately. It can serve as the basic model for braking and steering stability analysis.

(2) The original system has been transformed into the equivalent system by using the D'Alembert principle. The equilibrium points of the equivalent system are solved by the hybrid algorithm combining the genetic algorithm and sequential quadratic programming method. The bifurcation diagram of the equilibrium point with the braking torque is calculated. The results indicate that as the braking torque increases, the number of equilibrium points increases to three from one, and the system state changes to stable from unstable. The bifurcation characteristics have been confirmed by the phase portrait.

(3) The process of solving the stability region under steering and braking conditions has been determined, and the two-dimensional bifurcation parameter set (front wheel steering angle and braking torque) has been obtained for different longitudinal velocities. The three-dimensional stability region (longitudinal velocity, front wheel steering angle and braking torque) was fitted and verified.

(4) Stable regions of the system with and without inertia force have been solved using the energy dissipation method, and compared with the stability region obtained by the equivalent static bifurcation method. The results indicate that the equilibrium point bifurcation method proposed in this paper for steering and braking conditions can effectively solve the stability region of the equivalent system. The stability region of the equivalent system is almost the same as that of the original system without applying virtual force. When the limited braking torque is 500 N·m and the initial longitudinal velocity increases from 30 m/s to 50 m/s, the range of the stable region significantly decreases, and the absolute value of the front wheel steering angle at the boundary point changes from less than 0.02 rad to more than 0.02 rad.

Due to the danger of high-speed steering and braking conditions, as well as the extensive experiments required to explore the unstable region of the vehicle system, it has been difficult to achieve actual vehicle experimental verification so far. In the future, we will verify and analyze the results of steering and braking stability regions with a driving simulator.

This paper mainly studies vehicle steering and braking stability in planar motion, without considering the impact of the dynamic characteristics of the pitch and roll. In future research, factors such as pitch and roll will be considered to explore the effects of tire load changes and different braking modes on the system equilibrium point bifurcation and stability region.

Author Contributions: Conceptualization, X.W. and W.L.; methodology, X.W.; software, W.L.; validation, F.Z., Z.L. and W.B.; writing—original draft preparation, W.L.; writing—review and editing, W.L. and X.W. All authors have read and agreed to the published version of the manuscript.

Funding: This research was funded by the Key R&D Plan of Heilongjiang Province, grant number JD22A014 and by National Natural Science Foundation of China, grant number 52175497.

Data Availability Statement: Not applicable.

Conflicts of Interest: The authors declare no conflict of interest.

Nomenclature

T_b	braking torque
ω	actual body yaw rate
ω_e	expected body yaw rate
m	vehicle mass
l_f, l_r	distance from the front and rear wheels to the center of mass
L	sum of the front and rear wheelbases
K	vehicle stability factor
k_f, k_r	cornering stiffness of the front and rear wheels
B_f, B_r	stiffness factor of front and rear wheels
C_f, C_r	shape factor of the front and rear wheels
D_f, D_r	peak factor of front and rear wheels
v_y, v_x	lateral and longitudinal velocity of vehicle
ω_f, ω_r	angular velocity of front and rear wheels
T_{bf}, T_{br}	braking torque of front and rear wheels
F_{lf}, F_{lr}	longitudinal tire force of front and rear wheels
F_{sf}, F_{sr}	lateral tire force of front and rear wheels
R_e	wheel rolling radius
J	moment of inertia of the wheel
I_z	moment of inertia of the vehicle around the Z axis
δ_f, δ_r	steering angle of front and rear wheels
C_{air_x}, C_{air_y}	longitudinal and lateral air drag coefficient
A_{L_x}, A_{L_y}	longitudinal and lateral windward area of the vehicle
F_z	the total load of the front and rear wheels of the vehicle
$F_{\mu f}$, $F_{\mu r}$	the braking force of the front and rear wheel brake
F_{zf}, F_{zr}	the front and rear wheel load
ρ	air density
μ	adhesion coefficient
η	the braking torque distribution coefficient
g	gravity
x	longitudinal slip rate or sideslip angle
B, C, D, E	stiffness factor, shape factor, peak factor, curvature factor
α	tire sideslip angle
k	longitudinal slip
G_x, G_y	tire force combined slip correction parameters
F_{lf0}, F_{lr0}, F_{sf0}, F_{sr0}	longitudinal force and lateral force of front and rear tires in steady state
$r_{x,1}$, $r_{x,2}$, $r_{y,1}$, $r_{y,2}$	tire combined slip correction coefficients
ω_w	wheel rotation angular velocity
v_{wx}	longitudinal velocity at the wheel center in the tire coordinate system
α_f, α_r	sideslip angle of front and rear wheels
v_{xf}, v_{xr}	longitudinal velocity of the front and rear wheels in the tire coordinate system
v_{yf}, v_{yr}	lateral velocity of front and rear wheels in tire coordinate system
K_D	system parameter
v_{x1}, v_{y1}	longitudinal velocity, lateral velocity at the end of the simulation
ω_1,ω_{f1}, ω_{r1}	yaw rate, and front and rear wheel angular velocity at the end of the simulation

v_{x0}, v_{y0}	longitudinal velocity, lateral velocity at the start of the simulation
ω_0,ω_{f0}, ω_{r0}	yaw rate, and front and rear wheel angular velocity at the start of the simulation
W_b	the work done by the braking torque
$\Delta E_1, \Delta E_2, \Delta E_3$	the dissipation of wheel rotational energy caused by tire longitudinal slip, the energy dissipation caused by the lateral force generated by the cornering characteristics between the tire and the ground, the energy dissipation caused by air resistance
E_{wheel1}, E_{wheel0}	the rotational kinetic energy of the vehicle body at the end of the simulation time, the rotational kinetic energy of the vehicle body at the initial simulation time,
E_{body1}, E_{body0}	the sum of the lateral translational kinetic energy and yaw kinetic energy of the vehicle body at the end of the simulation time, the sum of the lateral translational kinetic energy and yaw kinetic energy of the vehicle body at the initial simulation time

References

1. Meng, F.; Shi, S.; Bai, M.; Zhang, B.; Li, Y.; Lin, N. Dissipation of energy analysis approach for vehicle plane motion stability. *Veh. Syst. Dyn.* **2021**, *60*, 4035–4058. [CrossRef]
2. Inagaki, S.; Kushiro, I.; Yamamoto, M. Analysis on vehicle stability in critical cornering using phase-plane method. *Jsae Rev.* **1995**, *2*, 216.
3. Ono, E.; Hosoe, S.; Tuan, H.D.; Doi, S.I. Bifurcation in vehicle dynamics and robust front wheel steering control. *IEEE Trans. Control Syst. Technol.* **1998**, *6*, 412–420. [CrossRef]
4. Liaw, D.-C.; Chiang, H.-H.; Lee, T.-T. Elucidating vehicle lateral dynamics using a bifurcation analysis. *IEEE Trans. Intell. Transp. Syst.* **2007**, *8*, 195–207. [CrossRef]
5. Shen, S.; Wang, J.; Shi, P.; Premier, G. Nonlinear dynamics and stability analysis of vehicle plane motions. *Veh. Syst. Dyn.* **2007**, *45*, 15–35. [CrossRef]
6. Sadri, S.; Wu, C.Q. Lateral stability analysis of on-road vehicles using Lyapunov's direct method. In Proceedings of the Intelligent Vehicles Symposium, Madrid, Spain, 3–7 June 2012.
7. Sadri, S.; Wu, C. Stability analysis of a nonlinear vehicle model in plane motion using the concept of Lyapunov exponents. *Veh. Syst. Dyn.* **2013**, *51*, 906–924. [CrossRef]
8. Della Rossa, F.; Mastinu, G. Straight ahead running of a nonlinear car and driver model—New nonlinear behaviours highlighted. *Veh. Syst. Dyn.* **2018**, *56*, 753–768. [CrossRef]
9. Mastinu, G.; Biggio, D.; Della Rossa, F.; Fainello, M. Straight running stability of automobiles: Experiments with a driving simulator. *Nonlinear Dyn.* **2020**, *99*, 2801–2818. [CrossRef]
10. Steindl, A.; Edelmann, J.; Plöchl, M. Limit cycles at oversteer vehicle. *Nonlinear Dyn.* **2020**, *99*, 313–321. [CrossRef]
11. Liu, L.; Shi, S.; Shen, S.; Chu, J. Vehicle Planar Motion Stability Study for Tyres Working in Extremely Nonlinear Region. *Chin. J. Mech. Eng.* **2010**, *23*, 185–194. [CrossRef]
12. Imani Masouleh, M.; Limebeer, D.J. Region of attraction analysis for nonlinear vehicle lateral dynamics using sum-of-squares programming. *Veh. Syst. Dyn.* **2018**, *56*, 1118–1138. [CrossRef]
13. Wang, X.; Shi, S.; Liu, L.; Jin, L. Analysis of driving mode effect on vehicle stability. *Int. J. Automot. Technol.* **2013**, *14*, 363–373. [CrossRef]
14. Shi, S.; Li, L.; Wang, X.; Liu, H.; Wang, Y. Analysis of the vehicle driving stability region based on the bifurcation of the driving torque and the steering angle. *Proc. Inst. Mech. Eng. Part D-J. Automob. Eng.* **2017**, *231*, 984–998. [CrossRef]
15. Shi, S.; Meng, F.; Bai, M.; Lin, N. The stability analysis using Lyapunov exponents for high-DOF nonlinear vehicle plane motion. *Proc. Inst. Mech. Eng. Part D-J. Automob. Eng.* **2022**, *236*, 1390–1400. [CrossRef]
16. Meng, F.; Shi, S.; Li, Y.; Zhang, B.; Yue, B.; Lin, N. Driving stability region solving method based on dissipation of energy. *Proc. Inst. Mech. Eng. Part D-J. Automob. Eng.* **2022**, *237*, 852–861. [CrossRef]
17. Olson, B.J.; Shaw, S.W.; Stépán, G. Stability and bifurcation of longitudinal vehicle braking. *Nonlinear Dyn.* **2005**, *40*, 339–365. [CrossRef]
18. Horiuchi, S.; Okada, K.; Nohtomi, S. Analysis of accelerating and braking stability using constrained bifurcation and continuation methods. *Veh. Syst. Dyn.* **2008**, *46*, 585–597. [CrossRef]
19. Chen, K.; Pei, X.; Ma, G.; Guo, X. Longitudinal/Lateral Stability Analysis of Vehicle Motion in the Nonlinear Region. *Math. Probl. Eng.* **2016**, *2016*, 3419108. [CrossRef]
20. Zhu, J.; Zhang, S.; Wang, G.; Zhang, W.; Zhang, S. Research on vehicle stability region under critical driving situations with static bifurcation theory. *Proc. Inst. Mech. Eng. Part D-J. Automob. Eng.* **2021**, *235*, 2072–2085. [CrossRef]
21. Lai, F.; Huang, C.; Ye, X. Analysis of Vehicle Driving Stability based on Longitudinal-lateral and Vertical Unified Dynamics Model. *Int. J. Automot. Technol.* **2022**, *23*, 73–87. [CrossRef]

22. Gürbüz, H.; Buyruk, S. Improvement of safe stopping distance and accident risk coefficient based on active driver sight field on real road conditions. *IET Intell. Transp. Syst.* **2019**, *13*, 1843–1850. [CrossRef]
23. Li, Z.; Chen, H.; Liu, H.; Wang, P.; Gong, X. Integrated Longitudinal and Lateral Vehicle Stability Control for Extreme Conditions With Safety Dynamic Requirements Analysis. *IEEE Trans. Intell. Transp. Syst.* **2022**, *23*, 19285–19298. [CrossRef]
24. Wang, Y.; Shi, S.; Gao, S.; Xu, Y.; Wang, P. Active Steering and Driving/Braking Coupled Control Based on Flatness Theory and A Novel Reference Calculation Method. *IEEE Access* **2019**, *7*, 180661–180670. [CrossRef]
25. Wang, J.; Luo, Z.; Wang, Y.; Yang, B.; Assadian, F. Coordination Control of Differential Drive Assist Steering and Vehicle Stability Control for Four-Wheel-Independent-Drive EV. *IEEE Trans. Veh. Technol.* **2018**, *67*, 11453–11467. [CrossRef]
26. Hucho, W.H. *Aerodynamics of Road Vehicles: From Fluid Mechanics to Vehicle Engineering*; Elsevier: Berlin/Heidelberg, Germany, 2013.
27. Yu, Z. *Automobile Theory*; China Machine Press: Beijing, China, 2009.
28. Wang, X.; Shi, S. Vehicle coupled bifurcation analysis of steering angle and driving torque. *Proc. Inst. Mech. Eng. Part D-J. Automob. Eng.* **2021**, *235*, 1864–1875. [CrossRef]
29. Pacejka, H.B.; Bakker, E. The magic formula tyre model. *Veh. Syst. Dyn.* **1992**, *21*, 1–18. [CrossRef]
30. Pacejka, H.B. *Tire and Vehicle Dynamics*; Elsevier: Amsterdam, The Netherlands, 2006.
31. Milani, S.; Marzbani, H.; Jazar, R.N. Vehicle drifting dynamics: Discovery of new equilibria. *Veh. Syst. Dyn.* **2022**, *60*, 1933–1958. [CrossRef]
32. Wang, X.; Shi, S.; Liu, L.; Jin, L. Vehicle Dynamics Equilibriums Solution Search Based on Hybridization of Genetic Algorithm and Quasi-Newton Method. *Chin. J. Mech. Engng.* **2014**, *50*, 120–127. [CrossRef]